**Please cite the Published Version**

**Data Access Statement:** The Supporting Information is available free of charge at https://pubs.acs.org/doi/10.1021/acsanm.5c02931.

# Sediment Recycling from the Preparation of $Ti_3C_2T_x$ for Strain Sensors

*Yanlin Li[1], Ruiqing Wu[1], Hao Zhang[1], Yixuan Han[1], Gang Lu[1,\*], Huangzhong Yu[2], Tomasz Liskiewicz[3], Dan Wu[1], Shengwei Shi[1,\*]*

[1]Hubei Key Laboratory of Plasma Chemistry and Advanced Materials, School of Materials Science and Engineering, Wuhan Institute of Technology, Wuhan 430205, China

[2]School of Physics and Optoelectronics, South China University of Technology, Guangzhou, 510641, China

[3]Faculty of Science and Engineering, Manchester Metropolitan University, Manchester M15 6BH, United Kingdom

*Corresponding authors: ganglu2019@163.com (G. Lu), shisw@wit.edu.cn (S. Shi)

**ABSTRACT:** Carbides/nitrides (MXenes) have been applied in various fields due to their unique two-dimensional structure and excellent conductivity. However, the sediments from the preparation of MXenes were often discarded without fully utilization, which generates huge waste and potential environmental pollution. Here, a strategy of turning the waste into treasure is proposed. Sediments from the preparation of $Ti_3C_2T_x$ have been effectively recycled, and strain sensors have been fabricated based on 25% $Ti_3C_2T_x$-$Ti_3AlC_2$/PVA composite film for human motion monitoring. The strain sensor shows fast response with a gauge factor of 5.53 under the strain less than 10%. We give a model to explain the operating mechanism of $Ti_3C_2T_x$-$Ti_3AlC_2$/PVA during the stretching process. The monitoring of human motions on fingers and wrists demonstrates extremely high sensitivity (response time <100 ms). Moreover, the strain sensor exhibits an excellent stability. This research opens the door for the future recycling of the sediments generated during the preparation of MXenes.

**Keywords:** $Ti_3C_2T_x$-$Ti_3AlC_2$, Recycle, Strain sensor, Sensitivity, Stability.

## 1. Introduction

Since Naguib *et al*. synthesized novel two-dimensional (2D) carbide $Ti_3C_2T_x$ in 2011, which was named MXenes due to its similar structure to that of 2D graphene[1], MXenes have been widely applied in various fields, such as energy storage[2,3], solar cells[4,5], electromagnetic interference

shielding[6,7], biomedicine[8], and telecommunications[9,10]. Particularly, with the rapid development of portable electronic devices and health monitoring systems, there is an increasing demand for low-cost, highly-sensitive, and long-durable sensors[11,12].

Sensors based on MXenes can be applied to detect a range of stimuli, such as pressure[13,14], strain[11,15–18], photon irradiation[19,20], electrochemical reactions[21,22], gas adsorption[23,24], humidity[25–27], pH[28,29], and temperature[30,31]. The adjustable layered structure of MXenes shows inherent advantages in pressure sensors, which can be widely used in smart fabrics[32], electronic skin[33,34], and healthcare monitoring[17,18,34]. Ma *et al*. reported a highly flexible and sensitive piezoelectric sensor based on multilayer MXene[35], and the gauge factor (GF) reached more than 180. Similarly, Zhang *et al*. developed a strain sensor using $Ti_3C_2T_x$/polyvinyl alcohol (PVA) hydrogel composites[36], which showed excellent tensile strength and high sensitivity, and its GF was 10 times higher than that of the original hydrogel. Zhao *et al*. developed an ultrasensitive self-powered mechanoluminescence smart skin based on the synergistic interaction of $Ti_3C_2T_x$ MXene/carbon nanotube, which was able to detect signals of ultra-low strains with ultra-high sensitivity, ultra-fast response time, excellent durability and stability[34]. It exhibited tunable and highly sensitive mechanoluminescent characteristics under the strain. Yang reported a sandwich-structured flexible strain sensor based on MXene/polypyrrole/hydroxyethylcellulose (MXene/PPy/HEC) conductive material and polydimethylsilane (PDMS) flexible matrix, which showed excellent sensing performances for monitoring human physiological activities, measuring external strain changes and real-time motion[37]. In addition, the MXene/PPy/HEC sensor could recognize different handwritten characters successfully, with the accuracy over 96%. These studies demonstrate the wide applicability and potential of MXenes in advanced sensor technologies.

Despite various promising applications, there are lots of waste generated during the etching of MAX to prepare MXenes[38], and generally they are highly viscous sediment and thrown away due to the difficulty to recycle[39], leading to significant economic losses and hindering the

commercialization of MXenes[40], nevertheless, the sediments contain multilayered $Ti_3C_2T_x$ MXenes with high conductivity and incompletely etched $Ti_3AlC_2$ with large strength. Recently, the utilization of $Ti_3C_2T_x$-$Ti_3AlC_2$ by-products has been found to be an effective way in different fields, such as supercapacitors[41], lithium-ion batteries[42], electromagnetic interference shielding[6], and sensors[43]. Liu *et al*. reported a simple method to prepare a highly sensitive ammonia sensor based on $Ti_3C_2T_x$/$Ti_3AlC_2$ in 2023[44]. As the gas sensing material, the $Ti_3C_2T_x$/$Ti_3AlC_2$ planar composite exhibited a high sensitivity, good selectivity and low detection limit for $NH_3$. Furthermore, the gas sensor showed good repeatability and long-term stability. Yang *et al*. presented a hydrogel made from a composite of MXene sediments and PVA[6]. The hydrogel was highly flexible and exhibited excellent electromagnetic interference shielding, which can be controlled by an internal biomimetic porous structure. In addition, the MXene sediment-based hydrogel was capable of detecting human motion and smart coding sensitively and reliably, but with a very small GF value of less than 2, highlighting the difficulty of achieving both high performance and sustainable fabrication in sediment-based sensors. Ma *et al*. proposed a strategy to combine MXene nanosheets with their sediments to build a smart wearable self-powered health monitoring system[43]. Particularly, the MXene sediments were used as printable ink and further utilized for pressure sensors, which showed excellent responsiveness in detecting motions or pulse signals with great potential in assessing health conditions. Unfortunately, there are still very few reports on the recycling of $Ti_3C_2T_x$-$Ti_3AlC_2$ for the application in strain sensors.

To address this gap, a strategy of turning waste into treasure is proposed by recycling $Ti_3C_2Tx$-$Ti_3AlC_2$ and integrating into sensors. The obtained $Ti_3C_2T_x$-$Ti_3AlC_2$/PVA composite film exhibits ultrahigh strength, excellent flexibility, as well as good electrical conductivity. Its application in strain sensors to monitor human motion also illustrates high sensitivity and excellent stability. Moreover, it contributes to the sustainability of MXene-based technologies by utilizing

waste in a way that not only addresses environmental concerns but also advances the performance of strain sensors.

## 2. Experimental

*Materials*：Hydrochloric acid（HCl）was obtained from Xilong Scientific Co., Ltd. LiF (99.9%) and dimethylsulphoxide (DMSO, 99.8%) was purchased from Shanghai Macklin Biochemical Co., Ltd. $Ti_3AlC_2$ (99.5%) was bought from Foshan XinXi Technology Co., Ltd. Polyvinyl alcohol (PVA) (99.0%) was provided by Sinopharm Chemical Reagent Co., Ltd.

*Etching of $Ti_3AlC_2$*: To prepare the etched $Ti_3AlC_2$, 2 g of LiF and 40 ml of 9 M HCl were added to a PTFE griffin beaker, followed by stirring. The beaker was then placed in an ice-water bath and 2 g of $Ti_3AlC_2$ was slowly added. The reaction temperature was set to 40 °C and kept for 48 h with continuous stirring. The resulting mixture was centrifuged at 5000 rpm for 10 min and the supernatant was discarded. Next, deionized water was added to the centrifuge tube, and the precipitate was shaken to thoroughly mix . This washing process was repeated several times until the pH of the supernatant approached 6. The collected precipitate was transferred to a beaker for futher intercalation.

*Intercalation of $Ti_3C_2T_x$*：Intercalating agent DMSO was added to the beaker containing the precipitate and then the mixture was stirred for 5 h, followed by ultrasonication for 1 h. Deionized water was then introduced to the intercalated sample, and centrifugation was performed at 10000 rpm for 10 min to remove the residual DMSO with three times washing cycles. The intercalated sample was subsequently shaken and centrifuged for 30 min at 3500 rpm with deionized water to collect the supernatant. This process was repeated until the supernatant became transparent. Finally, the collected supernatant was vacuum-filtered using a aqueous PTFE membrane (0.22 µm) to obtain a self-supporting $Ti_3C_2T_x$ membrane for further use. The remaining sediment in the centrifuge tube was collected for subsequent steps.

*Preparation of $Ti_3C_2T_x$-$Ti_3AlC_2$/PVA*: The final sediment, consisting of partially etched $Ti_3AlC_2$ and

multiple layers of $Ti_3C_2T_x$, was dried under vacuum. The sediment ($Ti_3C_2T_x$-$Ti_3AlC_2$) was then ground into particles with different weights (0.05, 0.10, 0.15, 0.20, 0.25 and 0.30 g). A desired amount of PVA was dissolved in 50 mL of deionized water and heated at 100 °C until fully melted. Meanwhile, 20 mL of deionized water was added to the $Ti_3C_2T_x$-$Ti_3AlC_2$ mixture to achieve uniform dispersion assisted by ultrasonication. The dispersion was then slowly added to the molten PVA solution while stirring to ensure even distribution. The mixed mixture was subsequently poured into a PTFE mold ($7.5 \times 10 \times 1$ $cm^3$) through gauze filtering. After natural drying for 48 h, $Ti_3C_2T_x$-$Ti_3AlC_2$/PVA composite films were obtained. The films were cut into $3 \times 1.5$ $cm^2$ strips for subsequent measurements.

*Characterizations and Measurements*: The morphology and layered structure of the samples were characterized by scanning electron microscopy (SEM, ZEISS GeminiSEM 300). The crystal structure was analyzed by X-ray diffraction (XRD, Bruker D8 ADVANCE). The functional groups were determined by Fourier transform infrared spectroscopy (FT-IR, Thermo Fisher Scientific Nicolet 6700).

Electrical signals were monitored by Keithley DMM6500 digital multimeter. The composite film was fixed onto a fixture, and mechanical tests were performed using a CMT series microcomputer-controlled electronic universal testing machine. Different bending radii were applied at a tensile rate of 50 mm/min, with the $Ti_3C_2T_x$-$Ti_3AlC_2$ content between 5 to 30 wt%.

The gauge factor (GF) is an important parameter to assess the sensitivity of the sensor, calculated as following [45]:

$$GF = \frac{S_2 - S_1}{\varepsilon_2 - \varepsilon_1} \tag{1}$$

$$S_i = \frac{R_i - R_O}{R_O} \tag{2}$$

Where $\varepsilon_2$ and $\varepsilon_1$ are strains at the end and beginning of the measurement, respectively. $S_2$ and $S_1$ represent the corresponding resistance variations at strains $\varepsilon_2$ and $\varepsilon_1$, $R_O$ and $R_i$ represent the

resistances before and after applying strain respectively.

For practical applications, the film was attached to the fingers and its resistance was measured during knuckle movements. Furthermore, the film was clung to the wrist to measure the influence of wrist joint movements on its conductivity.

## 3. Results and discussion

### 3.1 $Ti_3C_2T_x$-$Ti_3AlC_2$/PVA composite films

The preparation of $Ti_3C_2T_x$-$Ti_3AlC_2$/PVA composite film is illustrated in **Figure 1**. After etching and intercalation, high-quality layered $Ti_3C_2T_x$ can be obtained through repetitive centrifugations (**Figure S1**). The clay-like mixture that precipitates at the bottom of the centrifuge tube is thus extracted via filtration and vacuum-drying. Subsequently, the sediment, $Ti_3C_2T_x$-$Ti_3AlC_2$ mixture, is ground into powder and blended with PVA to obtain $Ti_3C_2T_x$-$Ti_3AlC_2$/PVA composite film.
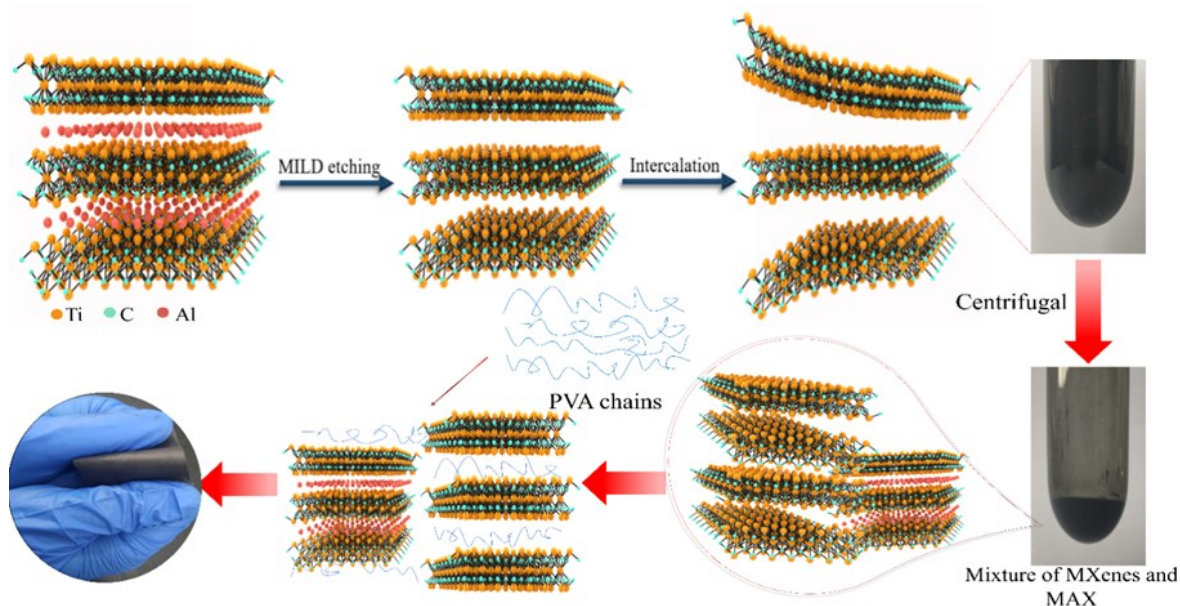


**Figure 1.** Schematic diagram of the preparation of $Ti_3C_2T_x$-$Ti_3AlC_2$/PVA film.

As shown from SEM images (**Figure S2**), most of $Ti_3C_2T_x$ nanosheets exhibit high-quality 2D structure with regular straight edges and intact morphology, indicating the successful etching of $Ti_3AlC_2$ and intercalation by DMSO [46]. XRD patterns of the intercalated $Ti_3C_2T_x$ are compared with those of the precursor $Ti_3AlC_2$ in **Figure 2**a. The characteristic peak at 38.74° which is corresponded to (104) planes nearly disappears in $Ti_3C_2T_x$, confirming the successful etching of the

Al layer from Ti$_3$AlC$_2$. In addition, the strong peak of (002) plane shifts from 9.52º to 6.21º, indicating that the interlayer spacing increases in Ti$_3$C$_2$T$_x$ compared to Ti$_3$AlC$_2$ due to the etching and intercalation effect [47]. SEM and XRD results collectively demonstrate the effectiveness of the etching and intercalation processes, resulting in high-quality Ti$_3$AlC$_2$ with good repeatability in the underlying precipitates.
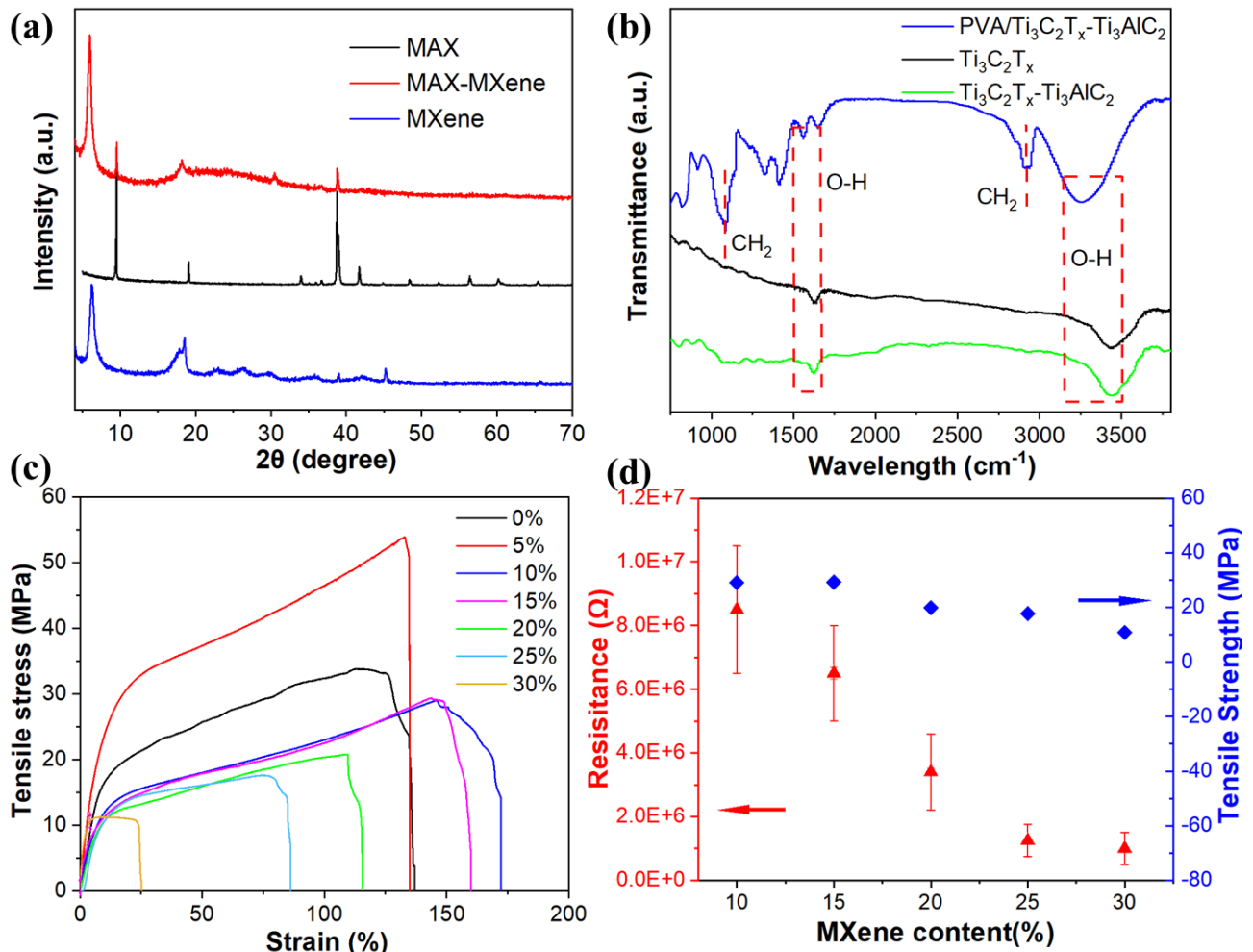


**Figure 2.** (a) XRD patterns of Ti$_3$AlC$_2$, Ti$_3$C$_2$T$_x$-Ti$_3$AlC$_2$ and Ti$_3$C$_2$T$_x$; (b) FT-IR spectra of Ti$_3$C$_2$T$_x$-Ti$_3$AlC$_2$/PVA, Ti$_3$C$_2$T$_x$ and Ti$_3$C$_2$T$_x$-Ti$_3$AlC$_2$; (c) Tensile stress-strain curves of composite films with different Ti$_3$C$_2$T$_x$-Ti$_3$AlC$_2$ contents; (d) Dependence of the resistance and tensile strength on the content of Ti$_3$C$_2$T$_x$-Ti$_3$AlC$_2$.

Figure 2a also presents XRD patterns for both Ti$_3$AlC$_2$ and Ti$_3$C$_2$T$_x$-Ti$_3$AlC$_2$. In comparison, the XRD pattern of Ti$_3$C$_2$T$_x$-Ti$_3$AlC$_2$ shows the same characteristic peaks of Ti$_3$AlC$_2$, along with a strong peak located at 6.2°, corresponding to the (002) plane, which is similar to that of DMSO-intercalated Ti$_3$C$_2$T$_x$. FT-IR spectra of Ti$_3$C$_2$T$_x$, Ti$_3$C$_2$T$_x$-Ti$_3$AlC$_2$ and the composite film are

given in Figure 2b. The O-H stretching vibration appears at 3430 cm$^{-1}$ in Ti$_3$C$_2$T$_x$ and Ti$_3$C$_2$T$_x$-Ti$_3$AlC$_2$, while a significant red shift to 3250 cm$^{-1}$ is observed in the Ti$_3$C$_2$T$_x$-Ti$_3$AlC$_2$/PVA film which may result from the hydrogen bonding between Ti$_3$C$_2$T$_x$-Ti$_3$AlC$_2$ and PVA. The same red-shift to lower wavenumbers was also observed for O-H vibration at 1550 cm$^{-1}$. In addition, symmetrical CH$_2$ vibration peaks of at 2940 cm$^{-1}$ and bending vibration peaks at 1090 cm$^{-1}$ are present in the composite film, which are specific to the PVA molecular chain and absent in Ti$_3$C$_2$T$_x$-Ti$_3$AlC$_2$.

The mechanical properties of the composite films are shown in Figure 2c. A small content (5%) of Ti$_3$C$_2$T$_x$-Ti$_3$AlC$_2$ significantly enhances the tensile strength at the same strain comparing to pure PVA, where Ti$_3$C$_2$T$_x$-Ti$_3$AlC$_2$ acts as reinforcing agent. The strong hydrogen-bonding interactions are crucial to this improvement, which exist in PVA molecular chains and between PVA and Ti$_3$C$_2$T$_x$-Ti$_3$AlC$_2$[6]. Generally, reinforcing agents are effective at low concentrations as well-dispersed rigid domains efficiently restrict polymer chain mobility and transfer stress, while they reduce the reinforcing effect at high contents, thus limiting the enhancement of tensile strength. When the content of Ti$_3$C$_2$T$_x$-Ti$_3$AlC$_2$ reaches 10%, the tensile strength of the composite film becomes lower than that of the pure PVA, which can be attributed to the onset of filler aggregation and microvoid formation. Beyond 10 %, the decline becomes more gradual as the interfacial disruption effect saturates, and it decreases to only 33% of the original when the Ti$_3$C$_2$T$_x$-Ti$_3$AlC$_2$ content is 30%. However, it is noteworthy that the elongation at break increases with Ti$_3$C$_2$T$_x$-Ti$_3$AlC$_2$ content up to 15%, reaching a maximum of 147.0% at 10%, which indicates that moderate filler content can enhance flexibility by promoting a more ductile fracture mode. Over the range from 0 to 15%, the composite film exhibits larger elongation at break than pure PVA. In addition, Young's modulus reaches the largest value of 3.5 GPa with 15% Ti$_3$C$_2$T$_x$-Ti$_3$AlC$_2$ content, and nearly all composite films show higher Young's modulus than pure PVA. This can be explained by the strong hydrogen bonding interactions between PVA and Ti$_3$C$_2$T$_x$-Ti$_3$AlC$_2$, which enhances

the mechanical properties despite the reduced interactions in PVA molecular chains at higher $Ti_3C_2T_x$-$Ti_3AlC_2$ concentrations. **Table 1** lists the mechanical properties of the composite films together with their resistances.

For a low $Ti_3C_2T_x$-$Ti_3AlC_2$ content (less than 5%), the composite films show insulating behavior similar to that of pure PVA film with very high resistance. As the content increases to 10%, the resistance of the composite film decreases to $8.50 \times 10^6$ $\Omega$, and when it continues to increase, the resistance decreases due to more and more conductive $Ti_3C_2T_x$-$Ti_3AlC_2$.

**Table 1.** Mechanical properties and resistance of $Ti_3C_2T_x$-$Ti_3AlC_2$/PVA composite films.

| Content /% | Elongation at break/% | Tensile strength /MPa | Young's modulus /GPa | Resistance ($\Omega$) |
|---|---|---|---|---|
| 0 | 126.4 | 33.5 | 1.6 | - |
| 5 | 134.8 | 53.9 | 2.1 | - |
| 10 | 147.0 | 29.0 | 2.1 | 8.50E+06 |
| 15 | 145.2 | 29.2 | 3.5 | 6.50E+06 |
| 20 | 109.7 | 19.9 | 1.1 | 3.40E+06 |
| 25 | 78.9 | 17.6 | 1.1 | 1.25E+06 |
| 30 | 24.0 | 10.9 | 2.0 | 1.00E+06 |

As the content of $Ti_3C_2T_x$-$Ti_3AlC_2$ increases, the electrical conductivity improves, and the mechanical properties gradually decrease. Therefore, a balance should be considered between the conductivity and mechanical properties for the strain sensor based on the composite film. From Table 1, it is evident that when the $Ti_3C_2T_x$-$Ti_3AlC_2$ content reaches 20%, the mechanical strength of the composite film starts to decrease significantly. When the content exceeds 25%, the enhancement in electrical conductivity becomes slowly. The resistance and tensile strength of composite films with $Ti_3C_2T_x$-$Ti_3AlC_2$ contents ranging from 10% to 30% are presented in Figure 2d. To achieve a balance between mechanical properties and conductivity, 25% $Ti_3C_2T_x$-$Ti_3AlC_2$ is selected for further strain sensors experiments, as it exhibits good conductivity, close to that of the 30% $Ti_3C_2T_x$-$Ti_3AlC_2$ film, while maintaining high tensile strength comparable to that of the 20% $Ti_3C_2T_x$-$Ti_3AlC_2$ film.

**Figure 3** presents the morphology of the composite films. At 10% $Ti_3C_2T_x$-$Ti_3AlC_2$, lumpy particles are observed to scatter within the PVA matrix (Figure 3a), and the layers stack without forming a continuously conductive network at higher magnification. At 20% content (Figure 3b), the lamella stacks and overlaps across each other, but some disconnections are still existed. When the content increases to 25% (Figure 3c), a relatively flat surface with a uniform distribution of $Ti_3C_2T_x$-$Ti_3AlC_2$ is observed, mainly resulting from 2D layered $Ti_3C_2T_x$. The evolution of the surface morphology of the composite films agrees quite well to their conductivity, as shown in Table 1. Here, the electrical conductivity of the composite films is mainly originated from $Ti_3C_2T_x$, while $Ti_3AlC_2$ contributes to the high strength, and PVA provides a uniform matrix to connect $Ti_3C_2T_x$-$Ti_3AlC_2$ layers. To further demonstrate the morphology evolution with the increasing content of $Ti_3C_2T_x$-$Ti_3AlC_2$, we also provide another batch of SEM images of films with different filler loadings (5, 10, 15, 20, 25, and 30 wt%) (**Figure S5**).
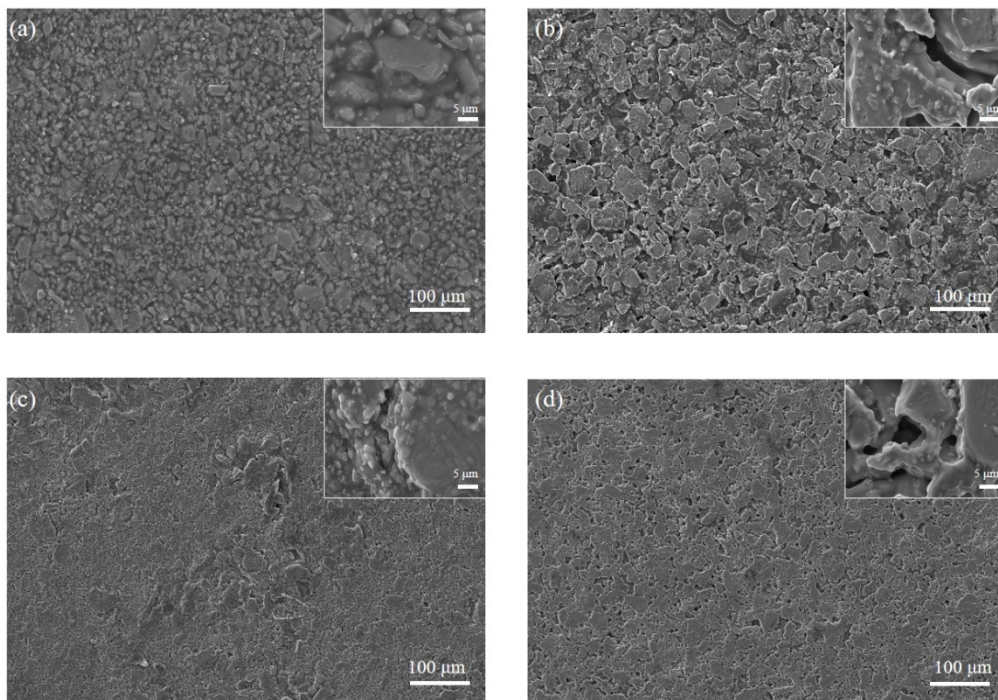


**Figure 3.** SEM images for composite films with different $Ti_3C_2T_x$-$Ti_3AlC_2$ contents, (a) 10%, (b) 20%，(c) 25%, and (d)30%. Inserted showed the partial enlarged image at high magnification.

### 3.2 Sensors based on $Ti_3C_2T_x$-$Ti_3AlC_2$/ PVA

The 25 wt% $Ti_3C_2T_x$-$Ti_3AlC_2$/PVA composite films are used to conduct the loading-unloading

experiments, which can be easily peeled off from the PTFE mold (**Figure S3**), and **Figure S4** indicates the operating under stretching stress on the universal testing machine.

As shown in **Figure 4**a, the stress-strain curves show significant hysteresis for all strains, with the hysteresis loops becoming more pronounced as the strain increases. For a strain of 50%, a significant stress loss occurs from the 1st to the 2nd cycle, but after that the stress loss decreases very slowly (Figure 4b). The hysteresis loop progressively overlaps with increasing cycles, indicating a good repeatability. Therefore, the dissipated energy during the cyclic tests remains relatively constant. To further confirm the repeatability, 100 successive loading-unloading cycles are measured at 5% strain, as indicated in Figure 4c. Noticeable hysteresis is observed during the initial cycles, indicating a certain degree of energy dissipation within the system. However, as the number of cycles increases, the stress-strain curves almost converge after the 6th cycle and the hysteresis loops exhibit quite good repeatability. By approximately the 100th cycle, the hysteresis loops become relatively stable, suggesting that internal energy loss is significantly reduced and the system reaches a steady state. This excellent resilience is attributed to abundant hydrogen bonding interactions in PVA molecular chains and between PVA and MXene nanosheets. The breaking and reorganization of the reversible bonding during the strain process result in excellent mechanical toughness of the composite films. Moreover, the $Ti_3C_2T_x$-$Ti_3AlC_2$/PVA composite film demonstrates excellent resilience with low energy loss, even at high strain exceeding 50%, highlighting its great potential in flexible strain sensors.

Furthermore, the dependence of the output current at 1 V on the bending radius is shown in Figure 4d. As the bending degree increases, the output current gradually decreases due to the enhanced resistance. A sharp reduction in output current occurs when the bending radius changes from 0.9 cm to 0.8 cm, and the current stabilizes thereafter. Despite significant bending, the composite film remains conductive, even when completely folded, due to the effective conductive connections formed by $Ti_3C_2T_x$-$Ti_3AlC_2$ components. In addition, the composite film shows a sharp

change in resistance during the bending process, with the resistance change rate exhibiting a significant response as the bending radius decreases (Figure 4e). For example, the resistance change rate is 17% for a bending radius of 1 cm, increasing to 60% for a bending radius of 0.8 cm. When the bending radius decreases further to 0.5 cm, the resistance change rate reaches as high as 80%. Notably, the resistance can easily recover to its initial value once the bending is released, indicating excellent flexibility and stability. Moreover, the GF value of the composite film can be obtained according to formula (1) from Figure 4f. The GF was 5.53 at small strains (less than 10%) and 3.00 at larger strains (greater than 10%), indicating high sensitivity as a strain sensor. Nevertheless, the film fails to function after stretching beyond 52%, as the internal conductive connections break under excessive strain.
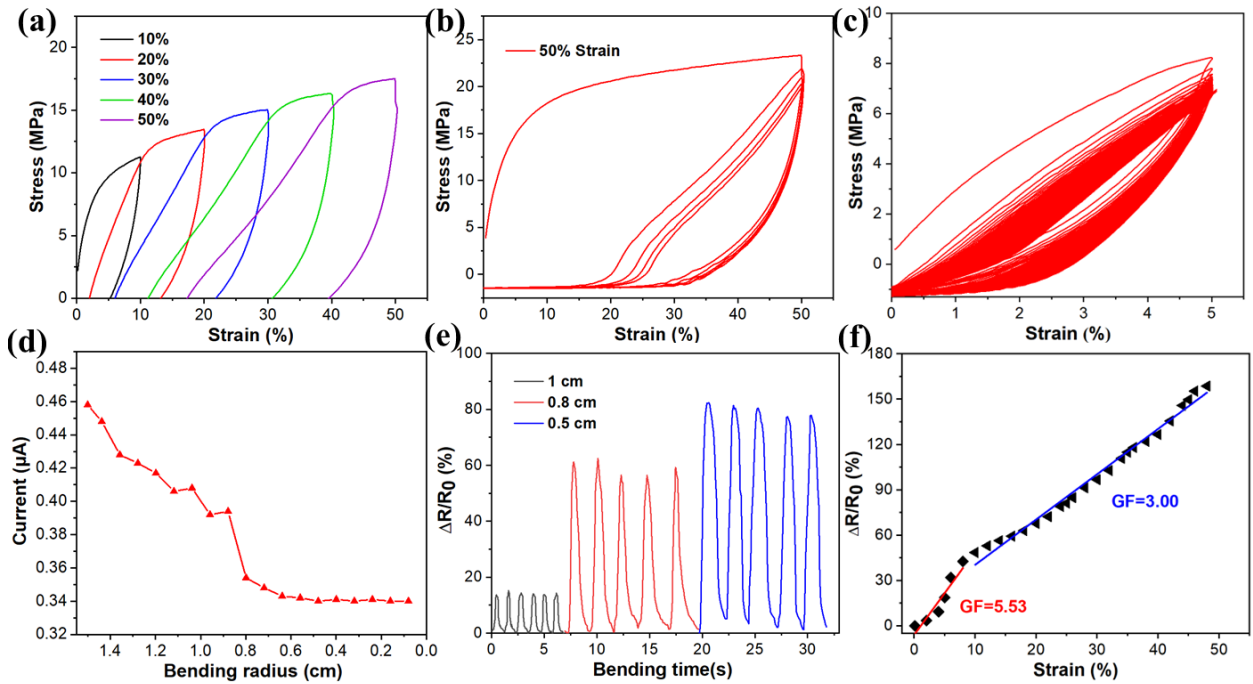


**Figure 4.** Sensors based on 25 wt% $Ti_3C_2T_x$-$Ti_3AlC_2$ /PVA film. (a) Stress-strain curves for loading-unloading tests under different strains; (b) 5 cycles of loading-unloading tests under 50% strain; (c) 100 cycles of loading-unloading tests under 5% strain; (d) Depending of output current on bending radius at 1V; (e) Resistance change rate at different bending radius; (f) Resistance change rate with the strain.

Although the GF still cannot compared with that of some state-of-the-art pure MXene-based sensors, it is higher than previous MXene sediment-based strain sensors[6]. More interestingly, it can reliably detect ultra-small strains with distinct and stable resistance response signal (such as 0.2 mm

in **Figure S6**). This makes it particularly suitable for precise monitoring in low-strain regimes, where many high-GF sensors may suffer from instability or noise at small deformations.

**Figure 5**a demonstrates the relative resistance variations of the $Ti_3C_2T_x$-$Ti_3AlC_2$/PVA composite film at different loading-unloading frequencies under 10% strain. For each loading-unloading cycle, the composite film shows a very fast response/recovery depending on the frequency, indicating high sensitivity as a strain sensor. Furthermore, the magnitude of resistance variation remains nearly the same across different frequencies, and the composite film operates very stably at the frequency from 0.1042 to 0.4167 Hz, showing excellent repeatability. The strong hydrogen bonding interactions between PVA and MXene nanosheets should contribute to the high sensitivity and excellent repeatability of the $Ti_3C_2T_x$-$Ti_3AlC_2$/PVA composite film[48].
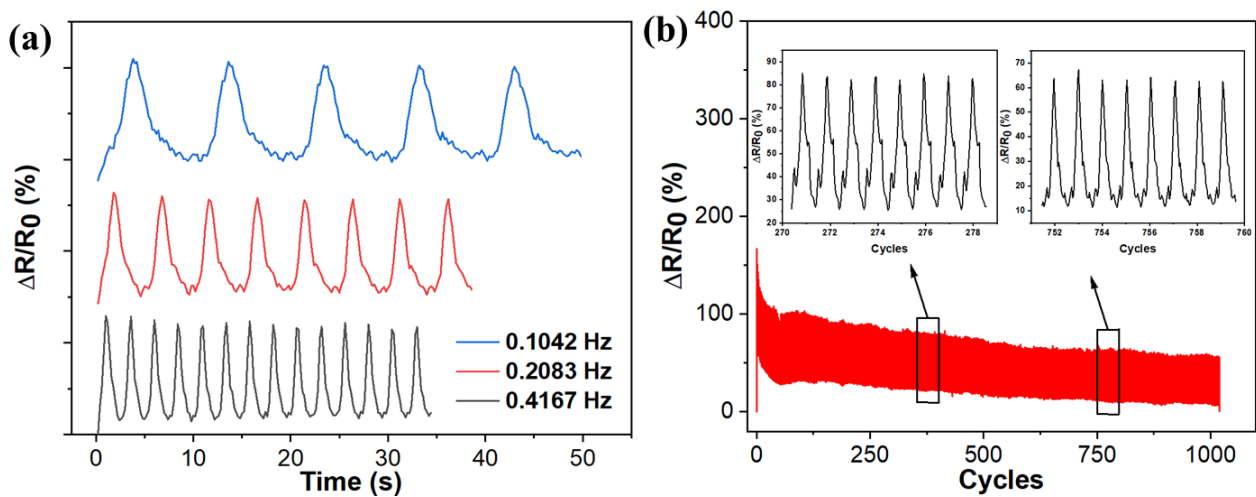


**Figure 5. (a)** Relative resistance variation under loading-unloading at different frequencies for 10% strain; (b) Cyclic stability of $Ti_3C_2T_x$-$Ti_3AlC_2$/PVA strain sensors under a strain of 10% and the inserted are the enlarged resistance change rate versus the cycles for indicated regions.

The cyclic stability is another important factor to ensure the commercial application of strain sensors for human motion monitoring. The strain sensor based on $Ti_3C_2T_x$-$Ti_3AlC_2$/PVA is investigated under 10% strain (Figure 5b), where the inserted images show the resistance change rate of specified regions throughout the entire cycle. The peak value of the relative resistance change rate is initially large during stretching, but it decreases rapidly and stabilizes after about 50-times stretching. After more than 1000-times stretching, although the resistance change rate

gradually shifts downward at both the peaks and troughs, the absolute value between the peaks and troughs remains nearly constant, indicating that the strain sensor operates very stably during the cycling measurement.
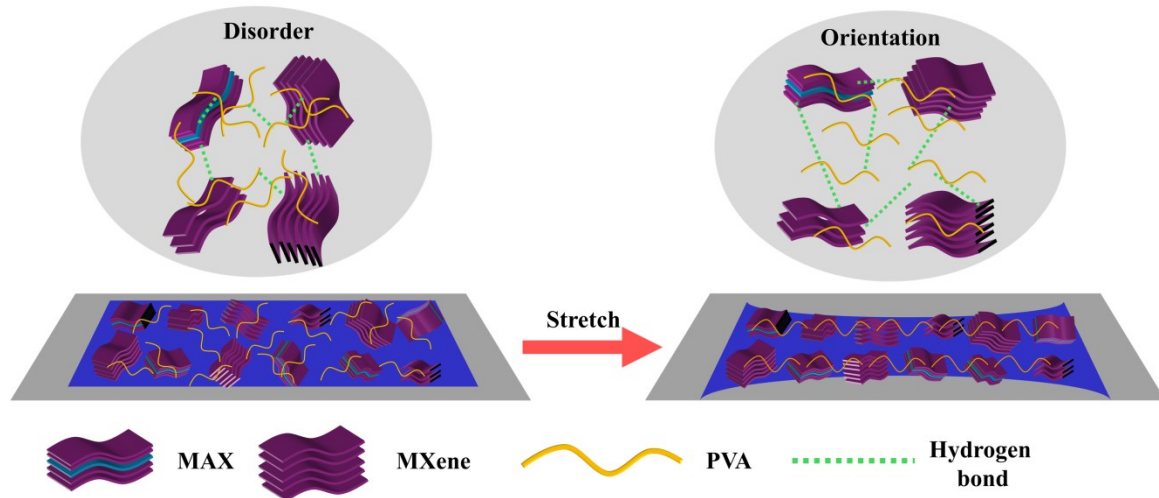


**Figure 6.** Operating mechanism of $Ti_3C_2T_x$-$Ti_3AlC_2$/PVA strain sensors.

### 3.3 Operating mechanism of $Ti_3C_2T_x$-$Ti_3AlC_2$/ PVA strain sensor

The operating mechanism of $Ti_3C_2T_x$-$Ti_3AlC_2$/PVA during the stretching process is illustrated in **Figure 6**. Before stretching, the MXene nanosheets and MAX 2D phases in $Ti_3C_2T_x$-$Ti_3AlC_2$ are randomly distributed and immobilized within the PVA matrix, leading to relatively high initial resistance due to the thick-film structure (50~100 μm) and the encapsulation of most conductive fillers inside the insulated polymer. When stress is applied, the $Ti_3C_2T_x$-$Ti_3AlC_2$ components orient, and they partially retain their orientation in the PVA matrix even after the stress is released, which improves the conductivity of the composite film. This behavior occurs because the PVA molecular chains are activated by heat generated during stretching, creating additional free volume for MXene nanosheets and MAX 2D phases to align. When the PVA chains cool upon release of the strain, the orientation is preserved. In addition, the stretching process promotes the crystallization of the PVA molecular chains, which also aid in maintaining the orientation of the $Ti_3C_2T_x$-$Ti_3AlC_2$ components. Therefore, the conductivity of the composite film is enhanced with stretching. Moreover, shoulder peaks observed during the cycles can be attributed to the competition between the breakage and

reconstruction of the conductive channels during the dynamic loading process[49]. As the number of stretching cycle increases, the resistance change rate gradually stabilizes, and the drift becomes negligible after 500 cycles, stabilizing between 875-1019 cycles as given in Figure 5b. The absolute values between the peaks and troughs of the electrical signals remain nearly almost constant, around 55%. Furthermore, as indicated in the insert, the resistance change rate remains stable from 270 to 280 cycles and from 751 to 760 cycles.

**3.4 Application of strain sensor in human motion monitoring**

The 25 wt% $Ti_3C_2T_x$-$Ti_3AlC_2$/PVA composite film is also demonstrated to effectively monitor human motion. **Figure 7**a-d show the resistance change rate with the bending of the index, middle, ring and pinky finger, respectively. The sensor exhibits a sharp increase in resistance with finger bending, and the response time is extremely short (＜100 ms), demonstrating very high sensitivity. In addition, due to variations in the flexibility and structure of different knuckles, the curves of resistance change rate show significant differences in their values, shapes and recovery, indicating the specificity of the sensor.

The resistance change rates of the sensor are also tested during the bending and twisting of the wrist joint (Figure 7e-f), which also exhibits fast response and high sensitivity. Notably, the resistance change rate of the wrist joint increases significantly after bending, but it takes longer to recover compared to the finger joint due to the large range of human motion. Moreover, the resistance change rate of wrist twisting differs significantly from that of wrist bending, initially decreasing rather than increasing after twisting. This interesting response could be due to the compression-induced cross-stacking effect of the unconnected $Ti_3C_2T_x$ inside the composite film, which reduces the resistance by 50%. During the twisting process, localized compressive stress facilitates the approach and even re-stacking of previously unconnected $Ti_3C_2T_x$ conductive domains, thereby increasing the number of conductive pathways and reducing the overall resistance. Additionally, the rapid response time supports the hypothesis of dynamic reconfiguration of the

conductive network under mechanical stress. During the recovery phase, partial misalignment and subsequent reconnection of the MXene nanosheets occur as the PVA matrix relaxes, resulting in a slight increase in the resistance change rate followed by another decrease. This reversible and repeatable response highlights the adaptability of the conductive network formed by the irregular, mixed-phase recycled fillers, and its ability to respond differently under tensile and torsional deformation modes. However, the recovery from wrist twisting occurs much faster than that from wrist bending.
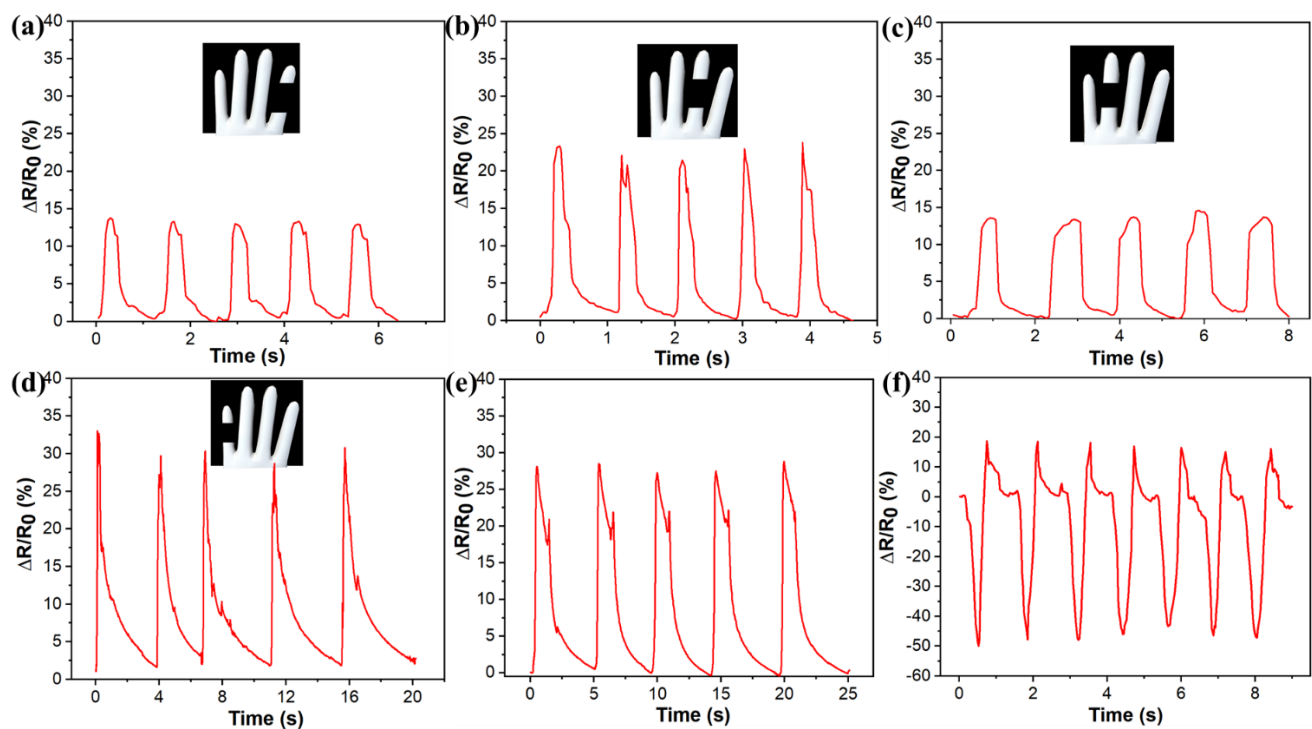


**Figure 7.** Resistance change rate for bending at knuckles: (a) index finger, (b) middle finger, (c) ring finger, (d) little finger. Resistance change rate for wrist: (e) bent, (f) twisted.

## 4. Conclusion

A strategy for converting waste into valuable material has been proposed to collect and recycle the sediments generated during the preparation of $Ti_3C_2T_x$. A 25% $Ti_3C_2T_x$-$Ti_3AlC_2$/PVA composite film has been fabricated as a highly sensitive strain sensor, demonstrating a GF value of 5.53 at strains less than 10%. Human finger and wrist motion monitoring reveals extremely high sensitivity, with a response time of less than 100 ms. Notably a remarkable growth in the resistance change rate

around 20% is observed during finger bending, with a 30% increase for wrist bending and a remarkable 70% increase for wrist twisting. Moreover, the strain sensor demonstrates an excellent stability. This study provides a promising approach for the effective recycling of sediments from MXenes preparation in future applications.

**Supporting Information**

SEM images of $Ti_3C_2T_x$ and $Ti_3C_2T_x$-$Ti_3AlC_2$; photos of MXene film, $Ti_3C_2T_x$-$Ti_3AlC_2$/PVA composite film and measurement process on the universal testing machine; relatively resistance change rate under very small strain.

**References**:

(1) Naguib, M.; Kurtoglu, M.; Presser, V.; Lu, J.; Niu, J.; Heon, M.; Hultman, L.; Gogotsi, Y.; Barsoum, M. W. Two-Dimensional Nanocrystals Produced by Exfoliation of $Ti_3AlC_2$. *Adv. Mater.* **2011**, *23* (37), 4248–4253.

(2) Li, X.; Huang, Z.; Shuck, C. E.; Liang, G.; Gogotsi, Y.; Zhi, C. MXene Chemistry, Electrochemistry and Energy Storage Applications. *Nat. Rev. Chem.* **2022**, *6* (6), 389–404.

(3) Anasori, B.; Lukatskaya, M. R.; Gogotsi, Y. 2D Metal Carbides and Nitrides (MXenes) for Energy Storage. *Nat. Rev. Mater.* **2017**, *2* (2), 16098.

(4) Han, T.; Zhu, W.; Wang, T.; Yang, M.; Zhou, Y.; Xi, H.; Zhong, P.; Chen, D.; Zhang, J.; Zhang, C.; et al. MXene-Interconnected Two-Terminal, Mechanically-Stacked Perovskite/Silicon Tandem Solar Cell with High Efficiency. *Adv. Funct. Mater.* **2024**, *34* (12), 2311679.

(5) Deng, B.; Lian, H.; Xue, B.; Song, R.; Chen, S.; Wang, Z.; Xu, T.; Dong, H.; Wang, S. Niobium-Carbide MXene Modified Hybrid Hole Transport Layer Enabling High-Performance Organic Solar Cells Over 19%. *Small* **2023**, *19* (23), 2207505.

(6) Yang, Y.; Wu, N.; Li, B.; Liu, W.; Pan, F.; Zeng, Z.; Liu, J. Biomimetic Porous MXene Sediment-Based Hydrogel for High-Performance and Multifunctional Electromagnetic Interference Shielding. *ACS Nano* **2022**, *16* (9), 15042–15052.

(7) Zhang, H.; Wan, J.; Wu, R.; Chen, Y.; Yu, H.; Shi, S. MXenes for Electromagnetic Interference Shielding: Insights from Structural Design. *Carbon* **2024**, *218* (10), 118716.

(8)  Yang, G.; Liu, F.; Zhao, J.; Fu, L.; Gu, Y.; Qu, L.; Zhu, C.; Zhu, J. J.; Lin, Y. MXenes-Based Nanomaterials for Biosensing and Biomedicine. *Coord. Chem. Rev.* **2023**, *479*, 215002.

(9)  Sarycheva, A.; Polemi, A.; Liu, Y.; Dandekar, K.; Anasori, B.; Gogotsi, Y. 2D Titanium Carbide (MXene) for Wireless Communication. *Sci. Adv.* **2018**, *4* (9), eaau0920.

(10)  Li, Y.; Tian, X.; Gao, S. P.; Jing, L.; Li, K.; Yang, H.; Fu, F.; Lee, J. Y.; Guo, Y. X.; Ho, J. S.; et al. Reversible Crumpling of 2D Titanium Carbide (MXene) Nanocoatings for Stretchable Electromagnetic Shielding and Wearable Wireless Communication. *Adv. Funct. Mater.* **2020**, *30* (5), 1907451.

(11)  Chae, A.; Murali, G.; Lee, S. Y.; Gwak, J.; Kim, S. J.; Jeong, Y. J.; Kang, H.; Park, S.; Lee, A. S.; Koh, D. Y.; et al. Highly Oxidation-Resistant and Self-Healable MXene-Based Hydrogels for Wearable Strain Sensor. *Adv. Funct. Mater.* **2023**, *33* (24), 2213382.

(12)  Du, C.; Zhang, H.; Liu, X.; Zhou, S.; Ma, Y.; Li, S. Flexible and Simply Degradable MXene-Methylcellulose Piezoresistive Sensor for Human Motion Detection. *ACS Appl. Mater. Interfaces* **2024**, *16* (10), 12996–13005.

(13)  Wang, Y.; Yue, Y.; Cheng, F.; Cheng, Y.; Ge, B.; Liu, N.; Gao, Y. Ti3C2Tx MXene-Based Flexible Piezoresistive Physical Sensors. *ACS Nano* **2022**, *16* (2), 1734–1758.

(14)  Wu, Z.; Wei, L.; Tang, S.; Xiong, Y.; Qin, X.; Luo, J.; Fang, J.; Wang, X. Recent Progress in $Ti_3C_2T_x$ MXene-Based Flexible Pressure Sensors. *ACS Nano* **2021**, *15* (12), 18880–18894.

(15)  Zhang, K.; Sun, J.; Song, J.; Gao, C.; Wang, Z.; Song, C.; Wu, Y.; Liu, Y. Self-Healing Ti3C2MXene/PDMS Supramolecular Elastomers Based on Small Biomolecules Modification for Wearable Sensors. *ACS Appl. Mater. Interfaces* **2020**, *12* (40), 45306–45314.

(16)  Liao, X.; Song, W.; Zhang, X.; Jin, H.; Liu, S.; Wang, Y.; Thean, A. V. Y.; Zheng, Y. An Artificial Peripheral Neural System Based on Highly Stretchable and Integrated Multifunctional Sensors. *Adv. Funct. Mater.* **2021**, *31* (24), 2101107.

(17)  Li, T.; Wang, Q.; Cao, Z.; Zhu, J.; Wang, N.; Li, R.; Meng, W.; Liu, Q.; Yu, S.; Liao, X.; et al. Nerve-Inspired Optical Waveguide Stretchable Sensor Fusing Wireless Transmission and AI Enabling Smart Tele-Healthcare. *Adv. Sci.* **2024**, *12* (4), 2410395.

(18)  Huang, Z.; Ge, C.; Li, S.; Cai, M.; Hui, Y.; Liao, X.; Zeng, Q. Biomimetic Pyrolytic MXene-Based Multifunctional Films with Multi-Level Structure for Wearable Piezoresistive Devices and Bioelectronics. *Adv. Funct. Mater.* **2025**, *35* (17), 2422374.

(19)  Chen, Y.; Dai, Y.; Bodepudi, S. C.; Liu, X.; Ma, Y.; Xing, S.; Di, D.; Tian, F.; Ming, X.; Liu, Y.; et al. High-Sensitive and Fast MXene/Silicon Photodetector for Single-Pixel X-Ray Imaging. *InfoMat* **2024**, *6* (9), e12596.

(20)  Kim, H.; Wang, Z.; Alshareef, H. N. MXetronics: Electronic and Photonic Applications of MXenes. *Nano Energy* **2019**, *60*, 179–197.

(21)  Shankar, S. S.; Shereema, R. M.; Rakhi, R. B. Electrochemical Determination of Adrenaline Using MXene/Graphite Composite Paste Electrodes. *ACS Appl. Mater. Interfaces*

**2018**, *10* (50), 43343–43351.

(22)    Pang, S. Y.; Wong, Y. T.; Yuan, S.; Liu, Y.; Tsang, M. K.; Yang, Z.; Huang, H.; Wong, W. T.; Hao, J. Universal Strategy for HF-Free Facile and Rapid Synthesis of Two-Dimensional MXenes as Multifunctional Energy Materials. *J. Am. Chem. Soc.* **2019**, *141* (24), 9610–9616.

(23)    Wu, M.; An, Y.; Yang, R.; Tao, Z.; Xia, Q.; Hu, Q.; Li, M.; Chen, K.; Zhang, Z.; Huang, Q.; et al. $V_2CT_x$ and $Ti_3C_2T_x$ MXenes Nanosheets for Gas Sensing. *ACS Appl. Nano Mater.* **2021**, *4* (6), 6257–6268.

(24)    Lee, E.; Vahidmohammadi, A.; Prorok, B. C.; Yoon, Y. S.; Beidaghi, M.; Kim, D. J. Room Temperature Gas Sensing of Two-Dimensional Titanium Carbide (MXene). *ACS Appl. Mater. Interfaces* **2017**, *9* (42), 37184–37190.

(25)    Muckley, E. S.; Naguib, M.; Wang, H. W.; Vlcek, L.; Osti, N. C.; Sacci, R. L.; Sang, X.; Unocic, R. R.; Xie, Y.; Tyagi, M.; et al. Multimodality of Structural, Electrical, and Gravimetric Responses of Intercalated MXenes to Water. *ACS Nano* **2017**, *11* (11), 11118–11126.

(26)    Wu, J.; Ai, W.; Long, Y.; Song, K. MXene-Based Soft Humidity-Driven Actuator with High Sensitivity and Fast Response. *ACS Appl. Mater. Interfaces* **2024**, *16* (21), 27650–27656.

(27)    Janica, I.; Montes-García, V.; Urban, F.; Hashemi, P.; Nia, A. S.; Feng, X.; Samorì, P.; Ciesielski, A. Covalently Functionalized MXenes for Highly Sensitive Humidity Sensors. *Small Methods* **2023**, *7* (8), 2201651.

(28)    Chen, X.; Sun, X.; Xu, W.; Pan, G.; Zhou, D.; Zhu, J.; Wang, H.; Bai, X.; Dong, B.; Song, H. Ratiometric Photoluminescence Sensing Based on $Ti_3C_2$ MXene Quantum Dots as an Intracellular PH Sensor. *Nanoscale* **2018**, *10* (3), 1111–1118.

(29)    Lv, Z.; Chen, X.; Yang, L.; Li, M.; Xia, C.; Luo, C.; Chao, M.; Yan, L. Bioinspired MXene Membranes with PH-Responsive Channels for High-Performance Water Purification. *ACS Appl. Polym. Mater.* **2024**, *6* (11), 6347–6357.

(30)    Jiang, X.; Kuklin, A. V.; Baev, A.; Ge, Y.; Ågren, H.; Zhang, H.; Prasad, P. N. Two-Dimensional MXenes: From Morphological to Optical, Electric, and Magnetic Properties and Applications. *Phys. Rep.* **2020**, *848*, 1–58.

(31)    Gao, F. L.; Liu, J.; Li, X. P.; Ma, Q.; Zhang, T.; Yu, Z. Z.; Shang, J.; Li, R. W.; Li, X. $Ti_3C_2T_x$ MXene-Based Multifunctional Tactile Sensors for Precisely Detecting and Distinguishing Temperature and Pressure Stimuli. *ACS Nano* **2023**, *17* (16), 16036–16047.

(32)    Li, Y.; Zhang, X. Electrically Conductive, Optically Responsive, and Highly Orientated $Ti_3C_2T_x$ MXene Aerogel Fibers. *Adv. Funct. Mater.* **2022**, *32* (4), 2107767.

(33)    Li, X.; Li, X.; Ting liu; Lu, Y.; Shang, C.; Ding, X.; Zhang, J.; Feng, Y.; Xu, F. J. Wearable, Washable, and Highly Sensitive Piezoresistive Pressure Sensor Based on a 3D Sponge Network for Real-Time Monitoring Human Body Activities. *ACS Appl. Mater. Interfaces* **2021**, *13* (39), 46848–46857.

(34)    Zhao, Y.; Gao, W.; Dai, K.; Wang, S.; Yuan, Z.; Li, J.; Zhai, W.; Zheng, G.; Pan, C.; Liu,

C.; et al. Bioinspired Multifunctional Photonic-Electronic Smart Skin for Ultrasensitive Health Monitoring, for Visual and Self-Powered Sensing. *Adv. Mater.* **2021**, *33* (45), 2102332.

(35)     Ma, Y.; Liu, N.; Li, L.; Hu, X.; Zou, Z.; Wang, J.; Luo, S.; Gao, Y. A Highly Flexible and Sensitive Piezoresistive Sensor Based on MXene with Greatly Changed Interlayer Distances. *Nat. Commun.* **2017**, *8*, 1207.

(36)     Zhang, Y. Z.; Lee, K. H.; Anjum, D. H.; Sougrat, R.; Jiang, Q.; Kim, H.; Alshareef, H. N. MXenes Stretch Hydrogel Sensor Performance to New Limits. *Sci. Adv.* **2018**, *4* (6), eaat0098.

(37)     Yang, C.; Zhang, D.; Wang, D.; Luan, H.; Chen, X.; Yan, W. In Situ Polymerized MXene/Polypyrrole/Hydroxyethyl Cellulose-Based Flexible Strain Sensor Enabled by Machine Learning for Handwriting Recognition. *ACS Appl. Mater. Interfaces* **2023**, *15* (4), 5811–5821.

(38)     Xu, J.; Peng, T.; Qin, X.; Zhang, Q.; Liu, T.; Dai, W.; Chen, B.; Yu, H.; Shi, S. Recent Advances in 2D MXenes: Preparation, Intercalation and Applications in Flexible Devices. *J. Mater. Chem. A* **2021**, *9* (25), 14147–14171.

(39)     Alhabeb, M.; Maleski, K.; Anasori, B.; Lelyukh, P.; Clark, L.; Sin, S.; Gogotsi, Y. Guidelines for Synthesis and Processing of Two-Dimensional Titanium Carbide ($Ti_3C_2T_x$ MXene). *Chem. Mater.* **2017**, *29* (18), 7633–7644.

(40)     Huang, P.; Ying, H.; Zhang, S.; Han, W. Q. Recent Advances and Perspectives of MXene Sediment: Composition, Morphology, Properties and Applications. *Coord. Chem. Rev.* **2024**, *515* (5), 215964.

(41)     Yuan, M.; Wang, L.; Liu, X.; Du, X.; Zhang, G.; Chang, Y.; Xia, Q.; Hu, Q.; Zhou, A. 3D Printing Quasi-Solid-State Micro-Supercapacitors with Ultrahigh Areal Energy Density Based on High Concentration MXene Sediment. *Chem. Eng. J.* **2023**, *451* (3), 138686.

(42)     Xu, H.; Zhu, W.; Sun, F.; Qi, H.; Zou, J.; Laine, R.; Ding, W. Turning Trash into Treasure: MXene with Intrinsic LiF Solid Electrolyte Interfaces Performs Better and Better during Battery Cycling. *Adv. Mater. Technol.* **2021**, *6* (3), 2000882.

(43)     Ma, J.; Yang, K.; Jiang, Y.; Shen, L.; Ma, H.; Cui, Z.; Du, Y.; Lin, J.; Liu, J.; Zhu, N. Integrating MXene Waste Materials into Value-Added Products for Smart Wearable Self-Powered Healthcare Monitoring. *Cell Rep. Phys. Sci.* **2022**, *3* (6), 100908.

(44)     Liu, Z.; Han, D.; Liu, L.; Li, D.; Han, X.; Chen, Y.; Liu, X.; Zhuo, K.; Cheng, Y.; Sang, S. Ultrasensitive Ammonia Gas Sensor Based on $Ti_3C_2T_x$/$Ti_3AlC_2$ Planar Composite at Room Temperature. *Sensor. Actuat. B* **2023**, *378* (3), 133149.

(45)     Yang, H.; Xiao, X.; Li, Z.; Li, K.; Cheng, N.; Li, S.; Low, J. H.; Jing, L.; Fu, X.; Achavananthadith, S.; et al. Wireless $Ti_3C_2T_x$ MXene Strain Sensor with Ultrahigh Sensitivity and Designated Working Windows for Soft Exoskeletons. *ACS Nano* **2020**, *14* (9), 11860–11875.

(46)     Xu, J.; Peng, T.; Zhang, Q.; Zheng, H.; Yu, H.; Shi, S. Intercalation Effects on the Electrochemical Properties of Ti3C2Tx MXene Nanosheets for High-Performance

Supercapacitors. *ACS Appl. Nano Mater.* **2022**, *5* (7), 8794–8803.

(47)     Qin, M.; Yuan, W.; Zhang, X.; Cheng, Y.; Xu, M.; Wei, Y.; Chen, W.; Huang, D. Preparation of PAA/PAM/MXene/TA Hydrogel with Antioxidant, Healable Ability as Strain Sensor. *Colloid. Surface. B* **2022**, *214* (3), 112482.

(48)     Lu, Y.; Qu, X.; Zhao, W.; Ren, Y.; Si, W.; Wang, W.; Wang, Q.; Huang, W.; Dong, X. Highly Stretchable, Elastic, and Sensitive MXene-Based Hydrogel for Flexible Strain and Pressure Sensors. *Research* **2020**, *2020*, 2038560.

(49)     Lin, L.; Liu, S.; Zhang, Q.; Li, X.; Ji, M.; Deng, H.; Fu, Q. Towards Tunable Sensitivity of Electrical Property to Strain for Conductive Polymer Composites Based on Thermoplastic Elastomer. *ACS Appl. Mater. Interfaces* **2013**, *5* (12), 5815–5824.